ACS OMEGA

Open Access



http://pubs.acs.org/journal/acsodf

Article

# Elucidating the Gas Phase Thermochemistry and the H-Atom Abstraction Reactions of Triethyl Phosphite

Zhihan Zhu, Frederick Nii Ofei Bruce, Yuke Gao, Chong-Wen Zhou, Yun Hin Taufiq-Yap, Fei Qin, Song Cheng, Henry Curran, and Yang Li*

Cite This: *ACS Omega* 2026, 11, 6023−6034

Read Online

ACCESS | Metrics & More | Article Recommendations | Supporting Information



**ABSTRACT:** Triethyl phosphite (TEPI), an organophosphorus compound, offers potential applications in flame-retardant materials, organic synthesis, homogeneous catalysis, agrochemicals, and pharmaceutical intermediate production. However, TEPI has received little attention compared to more extensively studied phosphates and phosphonates, with its thermal decomposition and chemical reactivity, particularly under combustion and high-temperature conditions, remaining largely unexplored. This study addresses that gap by analyzing the thermochemical properties and reaction kinetics of TEPI to clarify its combustion behavior and support the accurate modeling of its reaction pathways. In this study, the M06-2X/6-311++G(d,p) level of theory was used for geometry optimization, vibrational frequency calculations, and dihedral scans. The single-point energies (SPEs) of TEPI and its five radicals were calculated at the MP2/cc-pVXZ (X = D, T, or Q) and CCSD(T)/cc-pVXZ (X = D, T) levels of theory. We applied complete basis set (CBS) extrapolation to these energies to improve the accuracy and approximate the basis set limit. The bond dissociation energies (BDEs) of TEPI were calculated using single-point energies (SPEs) corrected with zero-point energies (ZPEs), as well as total energies at zero Kelvin (TEZK) obtained from an average of composite methods, including G3B3, G2, CBS-QB3, and G3B3. The thermochemical properties of TEPI and the rate constants for hydrogen atom abstraction (HAA) reactions with molecular oxygen, $O_2$, and various radicals: $^{\bullet}H$ (hydrogen), $^{\bullet}OH$ (hydroxyl), $^{\bullet}CH_3$ (methyl), $CH_3O^{\bullet}$ (methoxy), and $HO_2^{\bullet}$ (hydroperoxyl) were calculated using the Master Equation System Solver (MESS). The computed rate constants were further correlated with the corresponding energy barrier heights to elucidate their relationship. The results show that HAA from the secondary hydrogen site is more favorable than from the primary site, with the highest reaction rates observed for $^{\bullet}H$ and $^{\bullet}OH$ abstractions. With a kinetic mechanism still developing, additional reaction pathways such as hydrogen atom transfer and scission of various single bonds were estimated using rate constants derived by analogy. Furthermore, sensitivity analysis of the ignition delay time (IDT) confirmed the significance of HAA reactions, which control the initial consumption of TEPI. However, further refinement of the kinetic mechanism and experimental validation are necessary to fully confirm these reaction pathways and establish a robust model for TEPI's behavior under practical conditions. These findings offer fundamental insights and quantitative kinetic parameters into TEPI's reactivity, which serve as inputs for constructing detailed chemical kinetic models, thereby offering a quantitative basis for predicting its combustion behavior and optimizing its performance in flame-retardant applications.

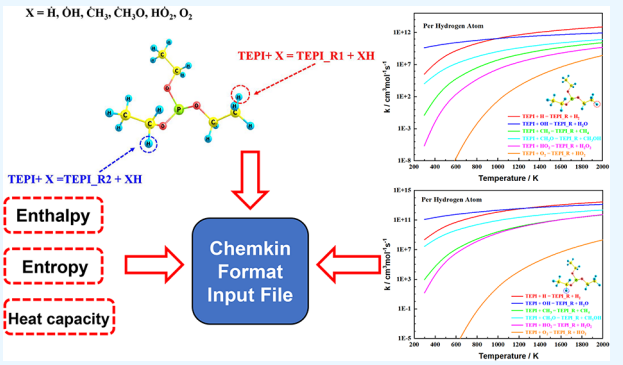


## 1. INTRODUCTION

Organophosphorus compounds (OPCs)[1] can be classified into phosphines, phosphonate esters, phosphoramides, and phosphate esters, with extensive applications across various fields. Phosphines[2] are commonly used as catalysts and ligands in organic synthesis, while phosphonate esters[3] are frequently utilized as herbicides. Phosphoramides[4] play a significant role in chemotherapy, inhibiting cancer cell proliferation in medical treatments. Phosphate esters[5] are flame retardants, plasticizers, and additives in industrial applications. OPCs typically exist in trivalent and pentavalent valence states. Trivalent phosphorus compounds adopt a trigonal pyramidal structure with three single bonds, commonly including phosphines and phosphite esters. Pentavalent phosphorus compounds generally exhibit a tetrahedral structure featuring one P═O double bond and three P═O single bonds, encompassing phosphonates and phosphates. Based on valence state, they can be categorized into the following two classes, as illustrated in Figure 1. Common organophosphorus compounds include trimethyl

Received: October 8, 2025
Revised: January 11, 2026
Accepted: January 13, 2026
Published: January 23, 2026

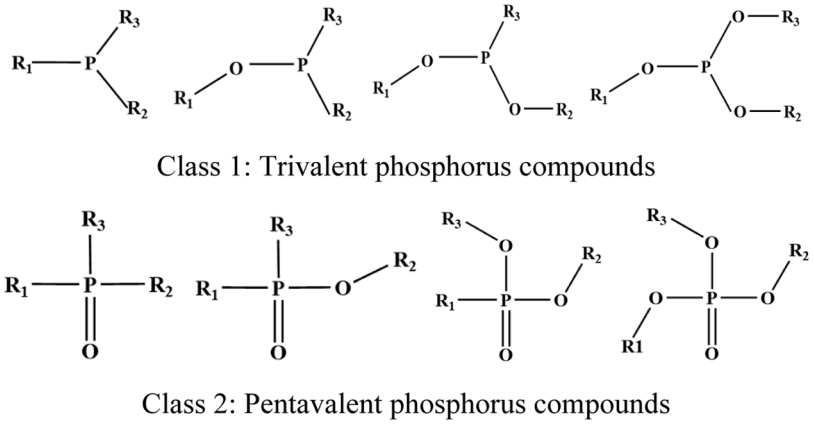


**Figure 1.** Classes of the OPCs. ($R_n$ is the substituents, alkyl, aryl, etc.)

phosphite (TMPI)[6] and triethyl phosphite (TEPI),[7] which belong to the first class of trivalent phosphorus; and trimethyl phosphate (TMP),[8,9] dimethyl methylphosphonate (DMMP),[10,11] and triethyl phosphate (TEP)[11,12] all belong to the second category of pentavalent phosphorus compounds.

Several studies have focused on elucidating the combustion behavior and functional applications of the OPCs. Lithium batteries pose a risk of thermal runaway[13] due to the highly flammable electrolyte. Traditional flame retardants[14−16] often sacrifice their electrochemical performance, and there is an urgent need for additives that combine efficient flame retardancy and electrochemical compatibility. In the context of energy storage, Li et al.[6] demonstrated that incorporating TMPI into electrolytes significantly enhances battery thermal resilience and improves cycling stability and rate capability. Merrow and Nogar[7] explored the photolysis of TEPI under pulsed $CO_2$ laser irradiation. Their study revealed that TEPI primarily undergoes C−O bond scission, generating intermediates such as $PO(OC_2H_5)_2$ and $C_2H_4$, further decomposing into smaller species such as HPO and PO. In terms of combustion mechanisms, Bruce and Li[8] combined quantum chemical calculations with MultiWell and MESS software to determine the bond dissociation energies (BDEs), thermochemical data, and hydrogen atom abstraction kinetics of TMP, providing essential theoretical support for its use in synthesis, combustion, and flame-retardant technologies. Complementarily, Badhuk and Ravikrishna[9] developed a simplified kinetic mechanism for TMP, identifying $PO_2$, HOPO, and $HOPO_2$ as key radical-scavenging intermediates in fire suppression. Werner and Cool[10] investigated DMMP's primary degradation pathways in varied combustion environments, revealing that hydrogen abstraction and molecular addition/substitution dominate its early stage reactions, particularly involving H and $^{\bullet}OH$ radicals. Sikes et al.[11] reported that at just 0.1% concentration, DMMP and TEP can reduce the laminar flame speed of $CH_4/O_2/N_2$ mixtures by approximately 30%. In hydrogen/air systems, the suppression effect of organophosphorus compounds (OPCs) increases with carbon content, with TEP and DMMP achieving 15% and 9% reductions in flame speed, respectively. Neupane et al.[12] conducted pyrolysis and oxidation experiments on TEP using shock tube and shock absorption spectroscopy techniques. Their modified kinetic model, based on AramcoMech 2.0[17] and LLNL mechanisms,[1,18] showed improved prediction accuracy for CO formation.

Among the OPCs, phosphites represent a relatively underexplored subclass, especially regarding their thermal decomposition and combustion-related reactivity. Phosphites are typically characterized by a central phosphorus atom bonded to three alkoxy groups, denoted as $P(OR)_3$, where R represents an alkyl or aryl group, such as methyl ($CH_3$), ethyl ($C_2H_5$), or phenyl ($C_6H_5$). These substituents significantly influence the physical and chemical properties of the molecule, including its volatility, reactivity, and thermal stability. Under thermal stress, phosphites can release phosphorus-containing degradation products that act as radical scavengers or flame inhibitors, contributing to their potential use in flame-retardant systems. However, despite this promise, phosphites have received considerably less attention than their phosphate and phosphonate counterparts, and their thermochemistry, decomposition mechanisms, and kinetic behavior remain insufficiently studied. In this context, triethyl phosphite (TEPI) is a model compound for investigating phosphite reactivity. Structurally, TEPI consists of a phosphorus atom covalently bonded to three ethyl ether groups ($-OC_2H_5$), forming a trigonal pyramidal geometry around the phosphorus center due to its lone electron pair. Figure 2 displays the optimized structure of TEPI with the lowest energy.

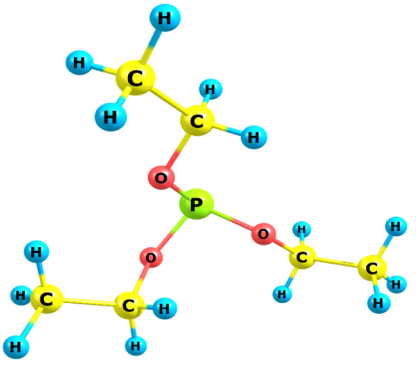

**Figure 2.** TEPI geometry structure.

Given its structure and potential for flame inhibition, TEPI may be considered a promising candidate for use as a flame-retardant additive, reactive intermediate, or multifunctional electrolyte component. To help close the knowledge gap surrounding phosphites, this study investigates the thermochemical properties of TEPI, calculates its BDEs, and analyzes its hydrogen atom abstraction (HAA) reactions with molecular


https://doi.org/10.1021/acsomega.5c10154
ACS Omega 2026, 11, 6023−6034

oxygen, $O_2$, and various radicals such as $^{\bullet}H$ (hydrogen), $^{\bullet}OH$ (hydroxyl), $^{\bullet}CH_3$ (methyl), $CH_3O^{\bullet}$ (methoxy), and $HO_2^{\bullet}$ (hydroperoxyl). The thermochemical analysis provides insight into the molecule's intrinsic stability and enthalpic profile, which is essential for modeling high-temperature behavior. BDE calculations allow for the identification of the most labile bonds and potential sites of radical formation, which is crucial for understanding decomposition pathways. HAA reactions, often the first step in radical-driven processes, are studied to determine the reactivity of TEPI under combustion-relevant conditions and to predict its influence on flame chemistry. Together, these investigations provide a comprehensive understanding of TEPI's energetic and kinetic behavior, offering valuable insights into the broader reactivity of phosphite compounds. This work supports the advancement of phosphite applications in combustion modeling, flame-retardant systems, and environmentally sustainable material design. Through quantitative analysis of energy barriers, reaction rate coefficients, and branching ratios, the study enriches the thermochemical data set of TEPI. This lays a theoretical foundation for the development of detailed reaction kinetic mechanisms.

## 2. THEORY AND METHODOLOGY

### 2.1. Computational Approach

Geometry optimization, frequency calculations, and dihedral angle scans were conducted employing the M06-2X functional[19] combined with the 6-311++G(d,p) basis set.[20,21] Low-frequency vibrational modes were analyzed, and internal rotations corresponding to these modes were scanned as a function of dihedral angles in 10° increments. For each transition state (TS), intrinsic reaction coordinate (IRC) calculations[22] were conducted to confirm the correct connectivity between reactants and products. The IRC paths were analyzed to monitor energy profiles along the reaction coordinates, identifying energy barriers and intermediate states. All calculations were executed using Gaussian 16 Revision C.01[23] software based on ab initio methods. To ensure consistency with the M06-2X functional, all species' zero-point energy (ZPE) and vibrational frequencies were scaled by 0.983 and 0.9698,[19] respectively, as recommended for the M06-2X functional by Zhao and Truhlar. Single-point energies (SPE) for all compounds were computed via second-order Møller–Plesset MP2/cc-pVXZ (where X = D, T, or Q) and coupled-cluster theory (CCSD(T))/cc-pVXZ (where X = D or T) methods. The obtained values were extrapolated to complete basis set limits using the prescribed correlation in eq 1.[24]

$$E_{CBS} = E_{CCSD/cc\text{-}pVTZ} + (E_{CCSD/cc\text{-}pVTZ} - E_{CCSD/cc\text{-}pVDZ}) \times 3^4/(4^4 - 3^4) + E_{MP2/cc\text{-}pVQZ} + (E_{MP2/cc\text{-}pVQZ} - E_{MP2/cc\text{-}pVTZ}) \times 4^4/(5^4 - 4^4) - E_{MP2/cc\text{-}pVTZ} + (E_{MP2/cc\text{-}pVTZ} - E_{Q/cc\text{-}pVDZ}) \times 3^4/(4^4 - 3^4) \quad (1)$$

The T1 diagnostic parameter[25] is an essential criterion for assessing the reliability of single-reference wave functions in high-level quantum chemical calculations. Initially developed in the context of coupled-cluster theory, T1 diagnostics are also widely applied in composite methods, such as G3 and CBS-QB3. Values of the T1 diagnostic help determine whether a molecule or transition state is suitable for treatment with single-reference methods, as deviations may indicate multi-reference character and potentially unreliable energy predictions. In this study, T1 diagnostics were computed for TEPI, its associated radicals (TEPI_$R_1$–$R_5$), and all relevant transition states involved in HAA reactions, using methods including G3, CBS-QB3, and CCSD(T) with various basis sets. These evaluations ensure the electronic structure methods' appropriateness and support the accuracy of the derived thermochemical and kinetic parameters.

The atomization method uses the average composite method of CBS-QB3,[26] G3,[27] G3B3,[27,28] and G2[29] to estimate the total energy at 0 K for each species. These composite methods inherently include electronic energy and zero-point vibrational energy (ZPVE), providing a consistent basis for thermochemical analysis. This selection of composite methods balances computational cost with accuracy, as demonstrated by prior studies showing that such approaches achieve desirable precision for thermochemical predictions.[30−32] Composite methods mitigate the high computational demands of quantum mechanical calculations (CCSD(T)/CBS) while retaining sufficient accuracy. The averaging protocol reduces systematic errors inherent in individual methods, enhancing reliability. Table 1 summarizes all of the quantum chemical computational methods used in this study.

**Table 1. All Quantum Chemical Computational Methods Used in the Study**

| Quantum chemical calculation | Method |
|---|---|
| Geometry, Frequency, Scan, and Intrinsic Reaction Coordinate (IRC) | M06-2X/6-311++G(d,p) |
| Single Point Energy (SPE) | CCSD(T)/cc-pVDZ |
| | CCSD(T)/cc-pVTZ |
| | MP2/cc-pVDZ |
| | MP2/cc-pVTZ |
| | MP2/cc-pVQZ |
| Total Energy at Zero Kelvin Energy (TEZK) | CBS-QB3/G3B3/G3/G2 |
| $H_{f,0K}$ | Atomization method |

The Master Equation System Solver (MESS) software[33] was employed in this study for both thermochemical and kinetic analysis. For thermochemistry, the PAC99 module within MESS was used to compute the standard thermodynamic properties of TEPI and its five associated radicals. These include enthalpies of formation ($H_f$), entropies ($S$), and temperature-dependent heat capacities ($C_p$), all evaluated from 298 to 1500 K. These calculations were based on the statistical thermodynamic treatment of vibrational, rotational, and translational partition functions, derived from quantum chemical data. MESS was further utilized for kinetics to solve the one-dimensional master equation and calculate temperature- and pressure-dependent rate constants. The kinetic framework incorporated the Canonical Transition State Theory (CTST) for quantum tunneling and anharmonic effects in the transition state. Additionally, the Rice–Ramsperger–Kassel–Marcus (RRKM) theory[34] was applied to determine unimolecular rate coefficients, coupled with an energy transfer model to simulate collisional energy redistribution in chemically activated species. Rate constants were computed over a temperature range of 298.15 to 2000 K, and the results were fitted to a modified Arrhenius expression, as


https://doi.org/10.1021/acsomega.5c10154
ACS Omega 2026, 11, 6023−6034

shown in eq 2, to enable convenient implementation in reaction mechanisms.

$$k = AT^{n}\left(-\frac{E_a}{RT}\right) \tag{2}$$

where $A$ denotes the pre-exponential factor, $T$ represents absolute temperature (K), $n$ is the exponent for temperature dependence, and $E_a$ indicates the energy barrier.

### 2.2. Bond Dissociation Energies (BDEs)

Bond dissociation energies (BDEs) are fundamental to assessing chemical bond strength and predicting the reactivity of TEPI. By comparing the total energies of products and reactants, BDEs were calculated for various bonds in TEPI, including C−H (primary and secondary), C−O, O−P, and C−C. These results provide critical insights into the molecule's thermal stability and reactive pathways. Figure 3 illustrates the dissociation of different bond types in TEPI, generating distinct radicals.

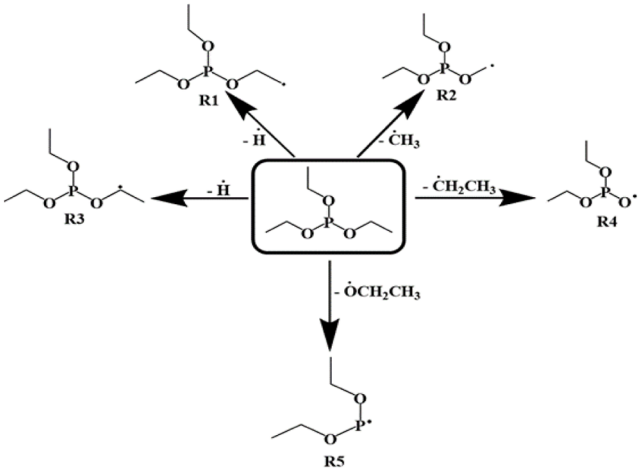


**Figure 3.** BDE of TEPI.

In this study, BDEs were determined by using two complementary approaches: The first method is total energy at zero Kelvin (TEZK),[8] using an average of composite methods—G3B3, CBS-QB3, G2, and G3B3—with all species optimized at the M06-2X/6-311++G(d,p) level. By obtaining the TEZK values of each species in Figure 3, different BDEs can be obtained via eq 3.

$$\begin{aligned}&\mathrm{TEZK}_{C_6H_{15}O_3P(\mathrm{TEPI})}\\ &\rightarrow 6\times\Delta_f H_{0K}(C_6) + 15\times\Delta_f H_{0K}(H_{15})\\ &\quad + 3\times\Delta_f H_{0K}(O_3) + \Delta_f H_{0K}(P_1) - (\mathrm{TAE}_0)\\ &\mathrm{BDE}_{\mathrm{TEZK}} = \mathrm{TEZK(B)} + \mathrm{TEZK(C)} - \mathrm{TEZK(A)}\end{aligned} \tag{3}$$

where $(\mathrm{TAE}_0)$ denotes total atomization energy. A represents TEPI, and B and C are free radicals formed after the breakage of any single bond in TEPI.

The second method employed SPE calculations corrected with ZPE, where the energies were extrapolated to the complete basis set (CBS) limit to calculate the BDE, as shown in eq 4 This extrapolation used CCSD(T) energies at the cc-pVDZ and cc-pVTZ levels, along with MP2 energies at the cc-pVDZ, cc-pVTZ, and cc-pVQZ levels, providing a high-accuracy estimate of the total energy for each species. Detailed calculations of different bonds have been listed in Supporting Information Tables S1 and S2.

$$\begin{aligned}&\mathrm{SPE} = \mathrm{ZPE}\times 0.9698 + E_{\mathrm{CBS}}\\ &\mathrm{BDE}_{\mathrm{SPE}} = [\mathrm{BDE}_{\mathrm{SPE}}(\mathrm{B}) + \mathrm{BDE}_{\mathrm{SPE}}(\mathrm{C}) - \mathrm{BDE}_{\mathrm{SPE}}(\mathrm{A})]\\ &\qquad\times \mathrm{au\ (in\ kcal/mol)}\end{aligned} \tag{4}$$

where A represents TEPI, B and C denote the radicals formed after cleavage of any single bond in TEPI, and 1 au (atomic unit) = 627.5095 kcal/mol.

### 2.3. H-Atom Abstraction (HAA) Reactions

To verify the combustion chemical properties of TEPI, we systematically investigated HAA reactions from two distinct hydrogen sites within the molecule.

This relationship can be expressed as shown in eq 5. In this process, the radical $R^{\bullet}$ approaches the hydrogen atom H at different sites of the molecule H−X. A transition state is formed between the radical and the hydrogen atom, with the hydrogen atom transferring from H−X to $R^{\bullet}$, forming a new molecule R−H and a new radical $X^{\bullet}$.

$$\mathrm{R} + (\mathrm{H{-}X}) = (\mathrm{R{-}H}) + \mathrm{X} \tag{5}$$

In this study, stable species, such as $O_2$ (oxygen), as well as radicals including $^{\bullet}H$ (hydrogen), $^{\bullet}OH$ (hydroxyl), $^{\bullet}CH_3$ (methyl), $CH_3O^{\bullet}$ (methoxy), and $HO_2^{\bullet}$ (hydroperoxyl), were used to abstract one hydrogen atom from the primary and secondary hydrogen positions in TEPI, respectively. These transition structures depict the molecular pathway between the starting materials and final species. The calculation of transition states can determine the specific reaction pathways, representing the highest-energy configurations during the reaction process and the energy barriers that must be overcome.

## 3. RESULTS AND DISCUSSION

### 3.1. Bond Dissociation Energy

The results of the BDE compared with ALFABET[35] are summarized in Supporting Information Table S3. Due to the varying accuracy of different computational methods, the results have minor differences. However, the overall trend in BDEs is consistent across the table: the C−O linkage exhibits minimal BDE (57.09−60.7 kcal/mol), indicating its preferential rupture initiates TEPI's thermal degradation. The C−C bond has the second-lowest BDE, ranging from 86.61 to 90.8 kcal/mol, indicating that C−C bond cleavage is also an essential pathway in the early stages of TEPI decomposition. Under high temperature and pressure, the preferential cleavage of C−O and C−C bonds indicates that TEPI's thermal stability is constrained by its weak bond energies, consistent with the initiation principles of radical chain reactions. When small radicals such as methyl ($-CH_3$) and ethyl ($-C_2H_5$), these intermediates can further react under high-temperature or fuel-rich conditions, eventually leading to substantial soot formation.

Existing research has yet to undertake systematic calculations of the BDEs for TEPI. To clarify the BDE characteristics of TEPI and elucidate its structure-energy correlation, this study compares the key chemical bond energies of TEPI with the corresponding bond energies of TEP (Triethyl phosphate), which possesses an additional P═O double bond compared to TEPI. The bond energies of the


https://doi.org/10.1021/acsomega.5c10154
ACS Omega 2026, 11, 6023−6034

C−C bond and the C−H bonds at the two sites in TEPI exhibit minimal deviation from their counterparts in TEP. Conversely, significant discrepancies exist in the BDEs of the C−O and O−P bonds between the two compounds. This discrepancy is possibly attributed to the presence of the P═O double bond in TEP molecules. (The validity of the analogy between TEP and TEPI has been demonstrated in the Supporting Information.)

Within TEPI molecules, C−O, C−C, and O−P bonds are more prone to cleavage than C−H bonds. Therefore, to comprehensively observe the modes and types of bond cleavage, this study employs the HAA reaction to investigate the cleavage of C−H bonds through radical abstraction methods. The C−H bonds have a relatively higher BDE compared to other bonds. From Figure 4, the differences in

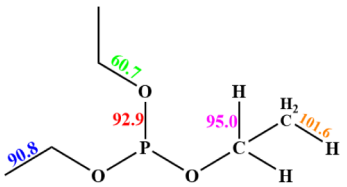


**Figure 4.** BDEs of TEPI (in kcal/mol, at $T$ = 0 K).

bond BDEs for various types of bonds can be observed, with the following order: primary hydrogen (101.4−102.1 kcal/mol) > secondary hydrogen (94.7−96.5 kcal/mol). The BDE of primary hydrogen is around 6.0 kcal/mol higher than that of secondary hydrogen, indicating that the C−H bonds at the secondary hydrogen positions are more likely to break.

### 3.2. Thermochemistry

Table 2 presents the thermochemical data calculated for TEPI and its five associated radicals in this study, alongside previously reported values from the available literature for comparison. For all systems examined, the calculated T1 diagnostic values remained within accepted thresholds—below 0.02 for closed-shell species, 0.03 for radicals, and 0.04 for transition states—indicating the reliability of the single-reference wave functions. Additional T1 values for TEPI and its five associated radicals are provided in Supporting Information Table S4, further confirming the high accuracy of the electronic structure calculations. Importantly, this work fills a significant gap in existing thermochemical databases, which lack comprehensive data for TEPI-derived radical species. The present study contributes to developing detailed reaction kinetic models by providing these missing thermodynamic parameters. It supports future mechanism generation for TEPI systems, particularly in combustion chemistry, atmospheric processes, and polymer degradation pathways.

### 3.3. Energy Barrier Comparisons

This study employed quantum computations to determine the HAA reactions on two hydrogen atom sites in TEPI, analyzing the potential energy surfaces (PES) and energy barriers for 12 reactions, as illustrated in Figure 5.

The reaction energy barriers for secondary hydrogen atoms are consistently lower than those for primary hydrogen atoms. This indicates that hydrogen atoms at the secondary positions are more prone to undergo HAA, which aligns well with the BDE results. Specifically, the C−H bonds at the secondary sites exhibit lower BDE values (indicating weaker bond strength) than those at the primary sites, thereby favoring bond cleavage and HAA at the secondary positions under similar reaction conditions. In Figure 5(b), the structure and energy corresponding to the reaction TEPI + $^{\bullet}$OH → TEPI_R + $H_2O$ are described. A weakly bound TEPI···$^{\bullet}$OH complex with a relative energy of −0.69 kcal/mol is formed between the reactants and the transition state, that is, TEPI + $^{\bullet}$OH → TEPI···$^{\bullet}$OH. This complex leads to the final product through the transition state, with the reaction progress depicted as TEPI···$^{\bullet}$OH → TEPI_R + $H_2O$. In the TEPI + $O_2$ → TEPI_R + $HO_2$ reaction depicted in Figure 5(f), similar dynamic behavior was observed, with the formation of weakly bound TEPI···$O_2$ complexes between the transition state and the products.

At low temperatures, the reaction rates of these radical-molecule reactions are influenced by van der Waals[32,40] forces, which form transient intermediates through weak intermolecular interactions, connecting reactants or products. van der Waals forces can stabilize the transition states' structure, lowering the energy barriers and accelerating reaction rates. This is typically manifested as local energy depressions (VDW wells) on the PES, located at the entrance or exit of the reaction path. For the TEPI + $^{\bullet}$OH reaction, the VDW wells are located at the entrance of the reaction channel, while for the TEPI + $O_2$ reaction, the VDW wells lie at the exit of the reaction channel. When calculating reaction rates, the influence of VDW forces proves crucial. Previous research indicates that VDW wells typically appear on the PES of $^{\bullet}$OH and $O_2$.

Supporting Information Table S5 summarizes the forward and reverse energy barrier heights for the hydrogen atoms at the primary and secondary hydrogen sites of TEPI. It can be observed that the forward energy barrier heights for the primary hydrogen sites range from 1.45 to 54.37 kcal/mol. In comparison, those for the secondary hydrogen sites range from 0.27 to 48.73 kcal/mol. Specifically, in the HAA reactions of TEPI with $^{\bullet}$OH, the forward barriers at the primary and secondary sites are 1.45 and 0.27 kcal/mol, respectively, indicating that these reactions are kinetically favorable and likely to proceed readily. In contrast, when TEPI reacts with $HO_2^{\bullet}$ and $O_2$ the forward energy barriers significantly increase. For $HO_2^{\bullet}$, the barriers are 22.87 kcal/mol (primary) and 14.21 kcal/mol (secondary), while for $O_2$, they reach 55.37 kcal/mol (primary) and 48.37 kcal/mol (secondary), suggesting that these reactions require higher energy input to proceed.

Notably, the reverse energy barriers exhibit a distinct trend. For reactions with $HO_2^{\bullet}$, the reverse barriers are 7.97 kcal/mol (primary) and 4.93 kcal/mol (secondary), whereas for reactions with $O_2$, the reverse barriers are exceptionally low (1.08 kcal/mol for primary-H and 1.06 kcal/mol for secondary-H), contrasting sharply with their high forward barriers. This significant asymmetry between forward and reverse barriers implies a strong thermodynamic preference for the reverse reaction pathway.

### 3.4. Rate Constant Calculations

The results for the HAA reactions of TEPI obtained in this study are summarized in Table 3, displaying the optimized Arrhenius coefficients ($A$, $n$, and $E_a$) for the HAA reactions of each hydrogen atom in the TEPI molecule. These parameters can be directly utilized to construct a combustion kinetic model for TEPI, providing significant insights into the HAA reactions. In the calculation process, the pre-exponential factor ($A$) ranged from $6.968 \times 10^{-5}$ to $5.0080 \times 10^{-4}$. The wide range of this parameter indicates an increased likelihood of


https://doi.org/10.1021/acsomega.5c10154
ACS Omega 2026, 11, 6023−6034

Table 2. Estimated Thermodynamic Values of TEPI and Related Species (kcal/mol for $H_f$, cal $K^{-1}$ $mol^{-1}$ for $S$ and $C_p$)[36−39]

| Species | Reference | Method | $H_f$ (298 K) | $S$ (298 K) | $C_p$ 300 | 400 | 500 | 600 | 800 | 1000 | 1500 |
|---|---|---|---|---|---|---|---|---|---|---|---|
| TEPI ($C_6H_{15}O_3P$) 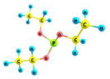 | Current study | Composite Method of CBS-QB3, G3, G3B3 and G2 | -192.43 | 113.01 | 49.07 | 60.70 | 71.28 | 80.18 | 92.60 | 101.77 | 115.84 |
| | NIST[36] | Group Additivity | -192.10 | 110.52 | 33.21 | 44.07 | 53.10 | 60.66 | 72.39 | 81.30 | 95.43 |
| | Neale and Williams[37] | Dewar bottle calorimetry method | -204.20 (liquid) | - | - | - | - | - | - | - | - |
| | Chernick[38] | Dewar bottle calorimetry method | -204.10 (liquid) | - | - | - | - | - | - | - | - |
| | Mortimer[39] | Calculation based on mean bond dissociation energies | -194.10 | - | - | - | - | - | - | - | - |
| TEPI_R1 ($C_6H_{14}O_3P$)  | Current study | Composite Method of CBS-QB3, G3, G3B3 and G2 | -147.30 | 123.75 | 50.70 | 60.87 | 70.18 | 78.04 | 89.15 | 97.66 | 110.90 |
| TEPI_R2 ($C_5H_{12}O_3P$)  | Current study | Composite Method of CBS-QB3, G3, G3B3 and G2 | -134.61 | 114.44 | 44.95 | 54.18 | 62.52 | 69.50 | 79.23 | 86.31 | 97.25 |
| TEPI_R3 ($C_6H_{14}O_3P$) 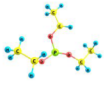 | Current study | Composite Method of CBS-QB3, G3, G3B3 and G2 | -147.62 | 118.79 | 51.98 | 64.13 | 74.52 | 82.63 | 92.52 | 100.05 | 111.89 |
| TEPI_R4 ($C_4H_{10}O_3P$) 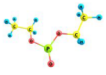 | Current study | Composite Method of CBS-QB3, G3, G3B3 and G2 | -163.98 | 103.40 | 36.20 | 43.90 | 51.00 | 57.13 | 66.19 | 72.91 | 83.15 |
| TEPI_R5 ($C_4H_{10}O_2P$) 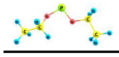 | Current study | Composite Method of CBS-QB3, G3, G3B3 and G2 | -133.50 | 98.98 | 33.09 | 40.33 | 46.97 | 52.70 | 61.17 | 67.57 | 77.45 |

molecular collisions, which makes the reaction more likely to occur. $E_a$ values for the primary HAA reactions ranged from $-2.84 \times 10^{02}$ to $5.29 \times 10^{04}$ kcal/mol, while those for the secondary HAA reactions ranged from $-3.95 \times 10^{02}$ to $4.71 \times 10^{04}$ kcal/mol.

**3.4.1. Rate on Primary Site.** Figure 6 compares the rate constants for the HAA reactions of TEPI, with all results based on the cleavage of each C−H bond. The results indicate that at a temperature of 200 K, $^{\bullet}$OH exhibits the highest rate constant, but $^{\bullet}$H surpasses it at 1000 K, primarily driven by entropy effects rather than energy barriers. At higher temperatures, the HAA reaction rates of all abstractants tend to converge and display similar trends.

In Figure 6, the reaction rates of TEPI with $^{\bullet}$H, $^{\bullet}$OH, $^{\bullet}CH_3$, and $CH_3O^{\bullet}$ are significantly higher than those with $HO_2^{\bullet}$ and $O_2$. This corresponds to the relative heights of the reaction energy barriers. Since the energy barriers for the reactions with $HO_2^{\bullet}$ and $O_2$ are relatively high, the reactions of TEPI with these two radicals require greater energy input, resulting in the slowest reaction rates.

**3.4.2. Rate on Secondary Site.** Figure 7 displays the HAA reaction rates for the secondary hydrogen atom in TEPI, exhibiting a trend similar to those of the primary hydrogen atom. The reaction rates of TEPI with $^{\bullet}$H and $^{\bullet}$OH are significantly faster than those with $^{\bullet}CH_3$, $CH_3O^{\bullet}$, $HO_2^{\bullet}$, and $O_2$ groups due to the effects of activation energy, $E_a$. The reaction rate plots reveal the same phenomenon: at lower temperatures, the reaction rate with $^{\bullet}$OH is the fastest, while around 1250 K, the reaction rate with $^{\bullet}$H becomes the fastest. The active groups $^{\bullet}CH_3$, $CH_3O^{\bullet}$, $HO_2^{\bullet}$, and $O_2$ exhibit increasing reaction rates with temperature, converging in the high-temperature region.

**3.4.3. Comparison of Different Site Abstractions by Similar Species.** Figure 8 compares rate constants for HAA reactions from two different hydrogen atoms under the same conditions for a given radical. It can be observed that the rate of the HAA reaction from secondary hydrogen is faster than


https://doi.org/10.1021/acsomega.5c10154
ACS Omega 2026, 11, 6023−6034

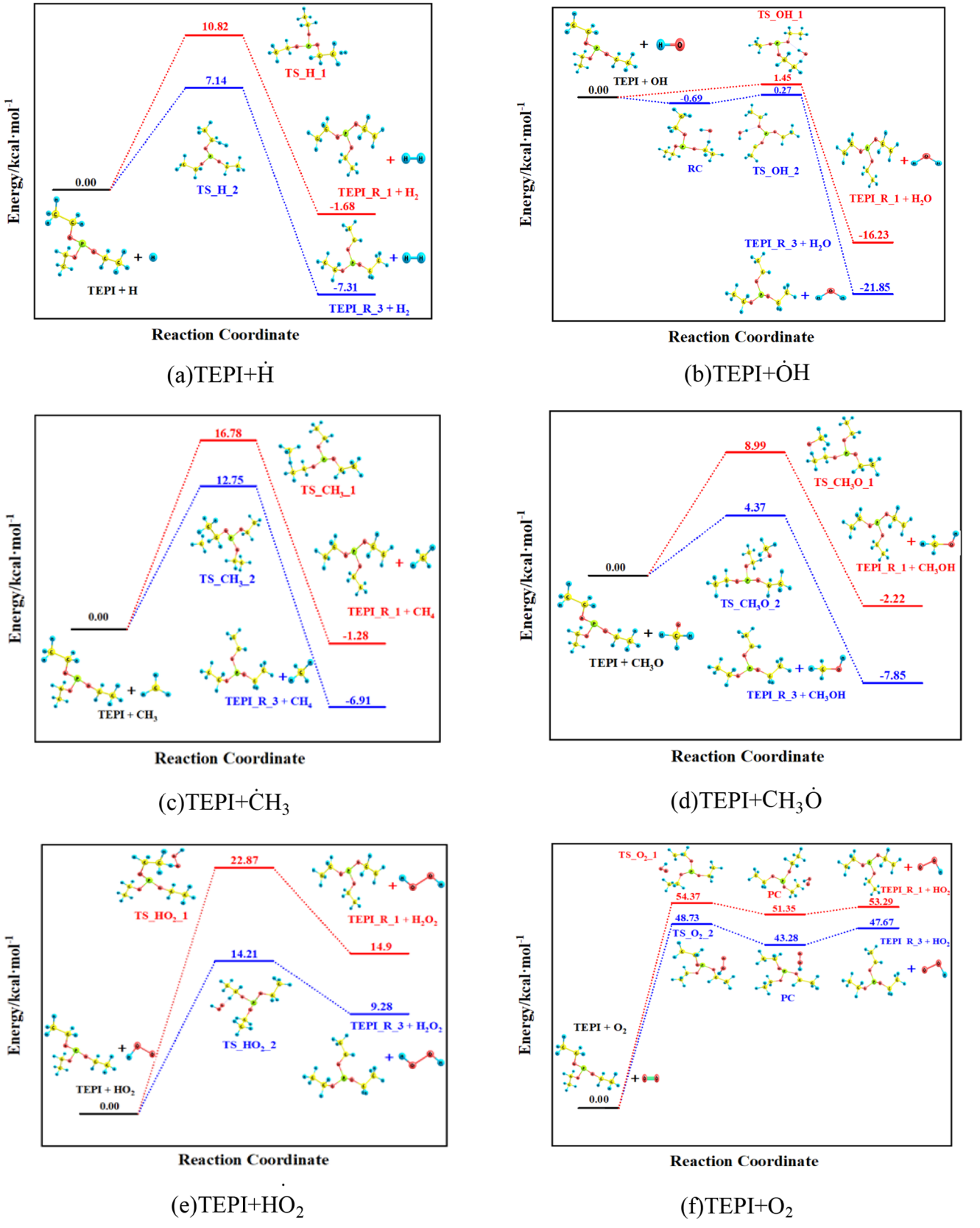


**Figure 5.** Potential energy surface for TEPI + X (X = •H, •OH, •$CH_3$, $CH_3O$•, $HO_2$•, $O_2$) abstraction reactions (in kcal/mol).

that from primary hydrogen. The reaction rates for abstracting secondary hydrogen atoms by •H, •$CH_3$, $CH_3O$•, $HO_2$•, and $O_2$ progressively approach those of primary hydrogen atoms with increasing temperature, as shown in Figure 8(a), (c), (d), (e), and (f). The abstraction rate of •OH from the secondary hydrogen site is 19.54 times higher than from the primary site and remains relatively constant across the entire temperature range. These results further confirm the analysis of BDE, as the



https://doi.org/10.1021/acsomega.5c10154
ACS Omega 2026, 11, 6023−6034

Table 3. Rate Constant Parameters for HAA Parameters (Total Hydrogen Atoms)

| Reaction | Primary H | | | Secondary H | | |
|---|---|---|---|---|---|---|
| | $A$ (mol cm s K) | $n$ | $E_a$ (cal/mol) | $A$ (mol cm s K) | $n$ | $E_a$ (cal/mol) |
| TEPI + $^{\bullet}H \rightarrow$ TEPI_R + $H_2$ | $3.94 \times 10^{03}$ | $3.36 \times 10^{00}$ | $7.48 \times 10^{03}$ | $7.59 \times 10^{03}$ | $3.27 \times 10^{00}$ | $3.93 \times 10^{03}$ |
| TEPI + $^{\bullet}OH \rightarrow$ TEPI_R + $H_2O$ | $7.70 \times 10^{02}$ | $3.03 \times 10^{00}$ | $-2.84 \times 10^{02}$ | $5.01 \times 10^{04}$ | $2.77 \times 10^{00}$ | $-3.95 \times 10^{02}$ |
| TEPI + $^{\bullet}CH_3 \rightarrow$ TEPI_R + $CH_4$ | $1.78 \times 10^{-04}$ | $4.99 \times 10^{00}$ | $1.17 \times 10^{04}$ | $6.97 \times 10^{-05}$ | $5.30 \times 10^{00}$ | $7.20 \times 10^{03}$ |
| TEPI + $CH_3O^{\bullet} \rightarrow$ TEPI_R + $CH_3OH$ | $6.04 \times 10^{-04}$ | $4.75 \times 10^{00}$ | $4.94 \times 10^{03}$ | $1.02 \times 10^{00}$ | $4.08 \times 10^{00}$ | $2.57 \times 10^{03}$ |
| TEPI + $HO_2^{\bullet} \rightarrow$ TEPI_R + $H_2O_2$ | $1.02 \times 10^{00}$ | $3.87 \times 10^{00}$ | $1.97 \times 10^{04}$ | $1.02 \times 10^{00}$ | $4.18 \times 10^{00}$ | $1.15 \times 10^{04}$ |
| TEPI + $O_2 \rightarrow$ TEPI_R + $HO_2^{\bullet}$ | $1.02 \times 10^{00}$ | $4.62 \times 10^{00}$ | $5.29 \times 10^{04}$ | $1.02 \times 10^{00}$ | $4.34 \times 10^{00}$ | $4.71 \times 10^{04}$ |

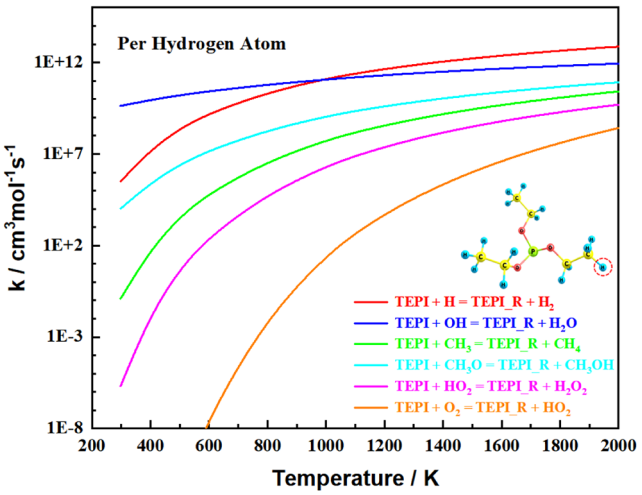


Figure 6. HAA reaction rate of primary hydrogen atoms in TEPI.

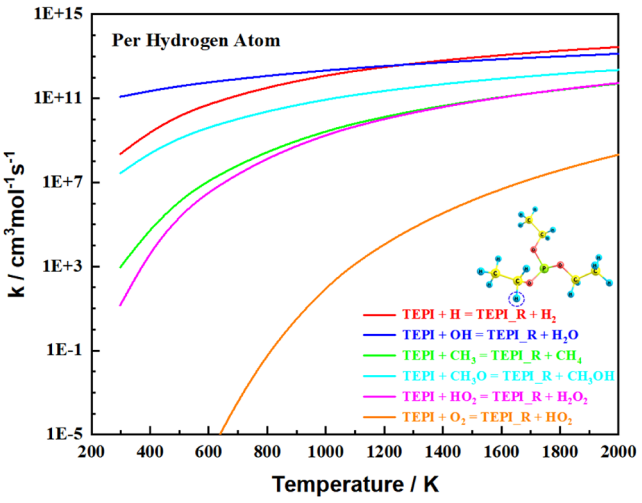


Figure 7. HAA reaction rate of secondary hydrogen atoms in TEPI.

C−H bond BDE of secondary hydrogen is lower than that of primary hydrogen, making HAA reactions more favorable in secondary positions. This indicates that secondary hydrogens will dominate the HAA reaction. In the TEPI + $O_2$ reaction, at low temperatures, the rate of the HAA reaction from secondary hydrogen is 32.1 times higher than that from primary hydrogen. As the temperature increases, the HAA rates at the two hydrogen sites gradually converge, and even at temperatures above 1400 K, the HAA rate at the primary hydrogen site becomes faster than that at the secondary hydrogen site. This may be due to the formation of van der Waals complexes, as mentioned earlier, which affect the reaction rates.

### 3.5. Comparison of TEP with TEPI

In the previous study, no computational data on the HAA of TEPI were available, so TEP, its phosphate, was used. This study compared the HAA reaction rates of various active groups ($^{\bullet}H$, $^{\bullet}OH$, $^{\bullet}CH_3$, $HO_2^{\bullet}$, and $O_2$) in the TEP mechanism obtained by Neupane et al.[41] through analogy with the DIMP mechanism developed by Glaude et al.,[18] as shown in Figure 9. The HAA reaction rate of TEP was faster for secondary hydrogen than for primary hydrogen. This is consistent with the results obtained from TEPI, where secondary hydrogen atoms dominate in the HAA reaction. The HAA reaction rate of TEP is generally faster than that of TEPI. Perhaps due to the electron-withdrawing effect of TEP containing a highly polar double bond P═O compared to TEPI, adjacent groups $O-C_2H_5$ are in an electron-deficient environment, weakening the C−H bond and making it easier for free radicals to abstract. In TEPI, P−O is a single bond with weak polarity, and lone pair electrons stabilize the $OCH_2CH_3$ group through conjugation, strengthening the C−H bond.

### 3.6. Ignition Delay Time Sensitivity Analysis

After completing the calculation of the reaction rate parameters, we constructed a complete kinetic model of TEPI combustion. The final constructed kinetic model includes approximately 278 species and 1655 reactions, of which approximately 50 species and 230 reactions are exclusive to TEPI. We integrated the TEPI submodels into the latest Galway C1 to C3 mechanism (C3MechV3.3Lite) developed by C3Mech[42] for simulating ignition delay time. To identify the kinetically significant reactions influencing the autoignition of TEPI, we performed a first-order brute-force sensitivity analysis of the IDT for individual reaction rate constants. This analysis was conducted at 1000 K and three different pressures: 1, 5, and 10 bar. "Brute force" sensitivity analyses were performed to investigate reactions significantly impacting model performance. Each reaction rate was increased and decreased by a factor of 2, which affects the predicted IDT. The sensitivity coefficient is defined as in eq 6.

$$S = \frac{\ln(\tau^+/\tau^-)}{\ln(k^+/k^-)} = \frac{\ln(\tau^+/\tau^-)}{\ln(2.0/0.5)} \quad (6)$$

where $\tau^+$ corresponds to the ignition delay time calculated with the increased rate constant, and $\tau^-$ corresponds to the ignition delay time calculated with the decreased rate constant.

A negative sensitivity coefficient indicates that increasing the rate constant decreases the ignition delay time; thus, the reaction promotes ignition. Conversely, a positive sensitivity suggests that the reaction inhibits ignition by consuming radicals or forming stable intermediates that slow chain branching. The kinetic mechanism used in this study is currently under development and refinement. Due to the limited availability of experimental or theoretical kinetic data


https://doi.org/10.1021/acsomega.5c10154
ACS Omega 2026, 11, 6023−6034

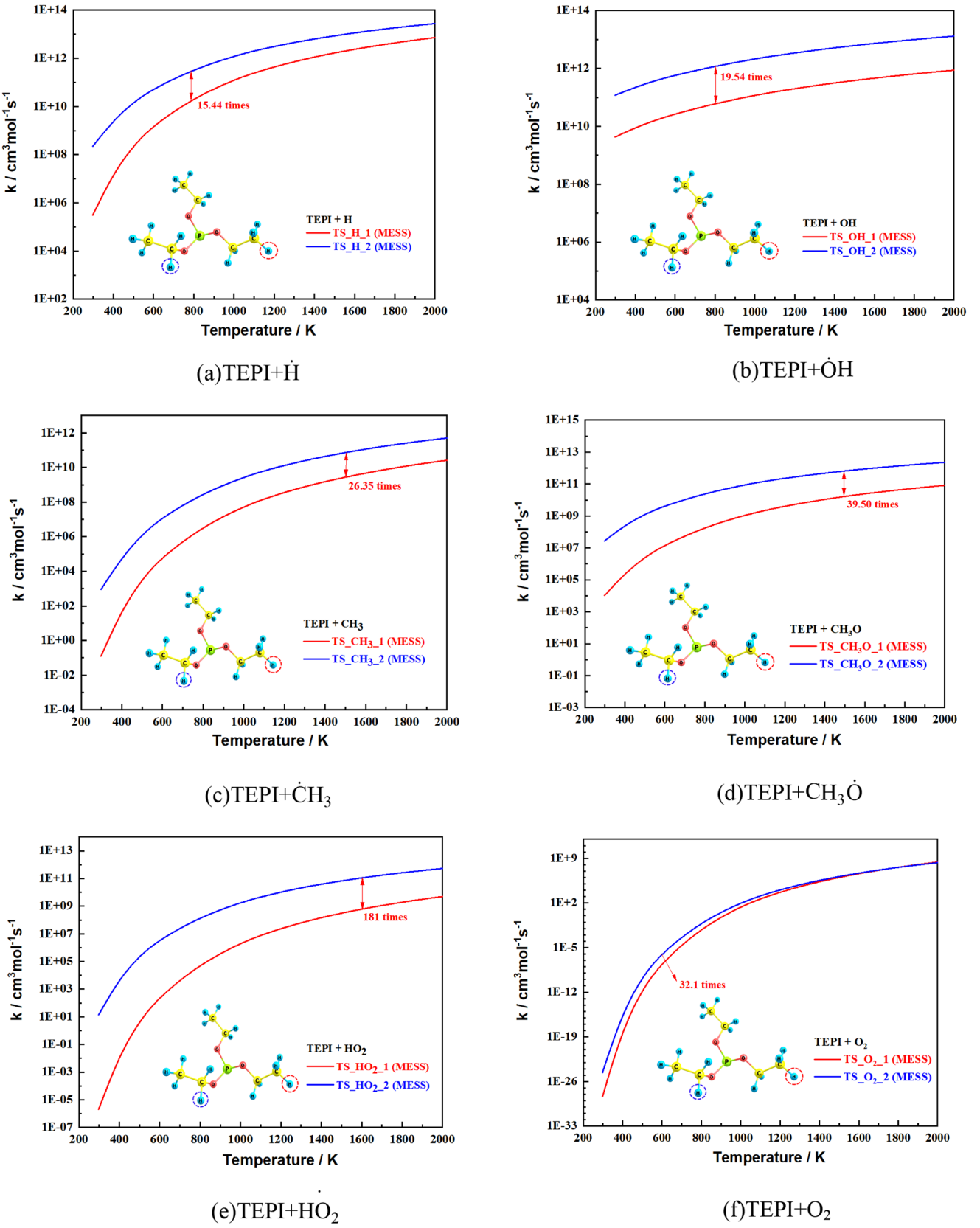


**Figure 8.** Comparison of the computed rate constants for abstracting different types of hydrogen atoms.

for phosphorus-containing species, especially those specific to TEPI, we used analogy-based estimation for several rate constants. In particular, triethyl phosphate (TEP) was employed as the primary analogue for estimating the rates of bond scission and radical reactions in TEPI. This choice is based on the structural similarity in P−C bonding environments between TEP and TEPI. However, the phosphate group in TEP introduces some chemical differences. These estimates



https://doi.org/10.1021/acsomega.5c10154
ACS Omega 2026, 11, 6023−6034

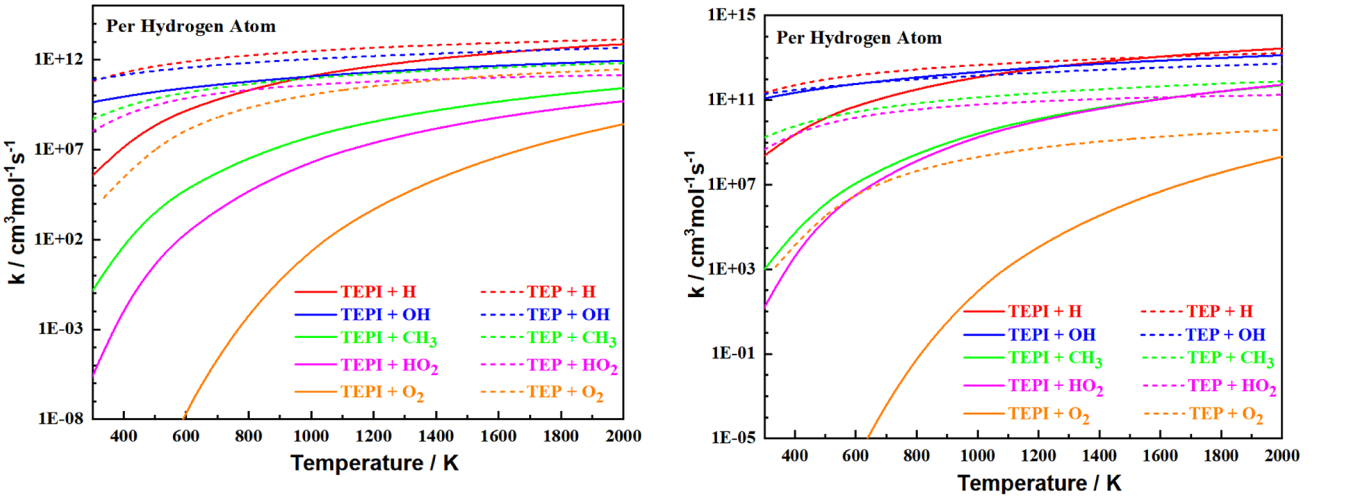


(a) Rate Comparison of primary H-atom (b) Rate Comparison of secondary H-atom

**Figure 9.** Comparison of HAA reactions between TEP and TEPI.

provide a preliminary framework that can be further refined with quantum chemical calculations and future experimental data. Figure 10 summarizes the sensitivity coefficients at each pressure.

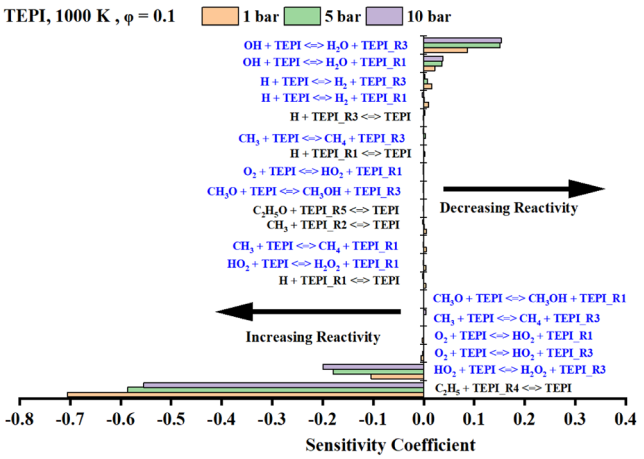


**Figure 10.** TEPI IDT sensitivity analysis (the HAA reactions are shown in blue color).

The reaction $C_2H_5$ + TEPI_R4 ⇌ TEPI shows the strongest negative sensitivity across all three pressures (−0.71 at 1 bar, −0.59 at 5 bar, and −0.55 at 10 bar), indicating that it plays a central role in ignition promotion. The decreasing sensitivity magnitude at higher pressures suggests the reduced importance of this pathway under compression, potentially due to altered radical lifetimes and competition with termination reactions. The reaction $HO_2^\bullet$ + TEPI ⇌ $H_2O_2$ + TEPI_R3 also displays significant negative sensitivity, becoming more influential as pressure increases. This suggests that peroxy pathways ($HO_2^\bullet$ and $H_2O_2$ formation) contribute to radical buildup and promote ignition in pressurized environments. Several abstraction reactions, especially those involving $^\bullet$OH and H radicals, exhibit positive sensitivities. For example, $^\bullet$OH + TEPI ⇌ $H_2O$ + TEPI_R3 increases sensitivity from +0.086 at 1 bar to +0.154 at 10 bar. H + TEPI ⇌ $H_2$+ TEPI_R3 similarly becomes more inhibitory at higher pressures. These reactions likely act as termination steps, removing radicals essential for chain branching and delaying ignition.

Some reactions exhibit sensitivity reversals depending on pressure. For instance, $^\bullet CH_3$ + TEPI ⇌ $CH_4$ + TEPI_R3 shifts from a slightly positive or neutral sensitivity at low pressure to a small negative value at 10 bar, indicating increased relevance in promoting ignition under compressed conditions. The sensitivity results provide critical guidance for mechanism development and model refinement: the strong influence of the $C_2H_5$ + TEPI_R4 and $HO_2^\bullet$ + TEPI pathways indicates a need for improved estimates or calculations of rate coefficients involving alkyl-phosphorus and peroxy-phosphorus intermediates. The increasing inhibition from $^\bullet$OH and H abstractions at high pressure underscores the importance of radical termination mechanisms in controlling ignition delay. These findings highlight the need for pressure-dependent kinetic expressions and thermodynamic consistency in modeling phosphorus combustion systems. Future efforts will include ab initio calculation of rate constants for the most sensitive unimolecular and bimolecular steps, incorporation of falloff and pressure-dependent reaction rate formulations where appropriate, and model validation against experimental IDT or flame speed data when available to constrain uncertainties in the phosphorus submechanism.

## 4. CONCLUSION

We investigated the thermochemistry and reaction kinetics of TEPI, with a focus on HAA with molecular oxygen, $O_2$, and various radicals such as $^\bullet$H (hydrogen), $^\bullet$OH (hydroxyl), $^\bullet CH_3$ (methyl), $CH_3O^\bullet$ (methoxy), $HO_2^\bullet$ (hydroperoxyl) using high-level ab initio quantum chemical calculations. The kinetics of these reactions were analyzed using MESS to obtain temperature-dependent rate constants over a wide thermal range.

The computational results revealed that HAA reactions from the secondary hydrogen site are consistently more favorable than those from the primary site. Among all studied pathways, $^\bullet$OH abstracting a secondary hydrogen atom showed the lowest forward energy barrier of 0.27 kcal/mol, indicating an exceptionally facile reaction. In contrast, $O_2$ abstracting a hydrogen atom from the


https://doi.org/10.1021/acsomega.5c10154
ACS Omega 2026, 11, 6023−6034

primary site exhibited a high forward energy barrier of 54.37 kcal/mol, making it kinetically unfavorable in the forward direction. However, the corresponding reverse barrier was only 1.06 kcal/mol, suggesting that the backward reaction is significantly more likely.

Temperature-dependent trends also emerged: at high temperatures, the TEPI + •H reaction proceeds at the fastest rate, whereas at low temperatures, the TEPI + •OH reaction dominates.

BDE calculations showed that the C−O bond has the lowest BDE (60.7 kcal/mol), indicating that C−O bond cleavage is likely the initial step in the thermal decomposition of TEPI. The C−H bonds exhibit the highest BDE and are the most resistant to cleavage; consequently, HAA reactions were calculated to observe the modes and types of bond cleavage.

Thermodynamic properties—including enthalpies, entropies, and heat capacities—were calculated for TEPI and its five radicals across a temperature range of 298 to 2000 K, enriching the thermochemical database for future kinetic modeling.

This study provides a detailed theoretical foundation for understanding TEPI's chemical behavior, particularly in combustion, atmospheric chemistry, and materials degradation. The results underscore the importance of HAA reactions as initiation steps in TEPI's reactivity and offer crucial insights for constructing accurate reaction mechanisms. While the findings are based on high-level quantum chemical computations, experimental validation remains essential. Future work will include experimental studies on TEPI's reactivity, and the kinetic data derived here will be integrated into reaction models developed using Chemkin for comparison with experimental combustion data.

## ■ ASSOCIATED CONTENT

### Data Availability Statement

All data generated or analyzed during this study are included in this article (and Supporting Information files).

### Supporting Information

The Supporting Information is available free of charge at https://pubs.acs.org/doi/10.1021/acsomega.5c10154.

Supporting Information 1: BDE results for the structures calculated in this study, T1 diagnostic values for all species involved, and HAA reaction barrier heights; Supporting Information 2: MESS input and output files for the TEPI HAA reactions; Supporting Information 3: mechanism files for TEPI (ZIP)

## ■ AUTHOR INFORMATION


### Corresponding Author

**Yang Li** − *National Key Laboratory of Solid Rocket Propulsion, School of Astronautics, Northwestern Polytechnical University, Xi'an 710072, China; Shenzhen Research Institute of Northwestern Polytechnical University, Shenzhen 518057, China;* orcid.org/0009-0003-8844-9346; Email: yang.li@nwpu.edu.cn

### Authors

**Zhihan Zhu** − *National Key Laboratory of Solid Rocket Propulsion, School of Astronautics, Northwestern Polytechnical University, Xi'an 710072, China; Shenzhen Research Institute of Northwestern Polytechnical University, Shenzhen 518057, China*

**Frederick Nii Ofei Bruce** − *National Key Laboratory of Solid Rocket Propulsion, School of Astronautics, Northwestern Polytechnical University, Xi'an 710072, China; Shenzhen Research Institute of Northwestern Polytechnical University, Shenzhen 518057, China;* orcid.org/0000-0003-3928-3928

**Yuke Gao** − *The 705 Research Institute, China State Shipbuilding Corporation, Xi'an 710075, China*

**Chong-Wen Zhou** − *Combustion Chemistry Centre, School of Biological and Chemical Sciences, Ryan Institute, MaREI, University of Galway, Galway H91 TK33, Ireland;* orcid.org/0000-0003-0845-988X

**Yun Hin Taufiq-Yap** − *Catalysis Science and Technology Research Centre, Faculty of Science, Universiti Putra Malaysia, Serdang, Selangor 43400, Malaysia;* orcid.org/0000-0002-3994-6720

**Fei Qin** − *National Key Laboratory of Solid Rocket Propulsion, School of Astronautics, Northwestern Polytechnical University, Xi'an 710072, China;* orcid.org/0000-0002-1440-1521

**Song Cheng** − *Department of Mechanical Engineering, The Hong Kong Polytechnic University, Kowloon 999077, Hong Kong;* orcid.org/0000-0001-6494-8659

**Henry Curran** − *Combustion Chemistry Centre, School of Biological and Chemical Sciences, Ryan Institute, MaREI, University of Galway, Galway H91 TK33, Ireland;* orcid.org/0000-0002-5124-8562

Complete contact information is available at: https://pubs.acs.org/10.1021/acsomega.5c10154



### Funding

The authors want to acknowledge support from the National Natural Science Foundation of China (NSFC) (22375165), the Shenzhen Science and Technology Program (JCYJ20240813150726034), and the IFS Collaborative Research Project (J24I078).

### Notes

The authors declare no competing financial interest.


## ■ ACKNOWLEDGMENTS

The authors acknowledge the funding support: National Natural Science Foundation of China (22375165). The author also acknowledges the assistance and support provided by Xuan Ren, Ruining He, Siyu Cheng, Mengmeng Jia, and Xin Bai from Northwestern Polytechnical University during the computational processes.

## ■ REFERENCES


(1) Glaude, P. A.; Curran, H. J.; Pitz, W. J.; Westbrook, C. K. Kinetic Study of the Combustion of Organophosphorus Compounds. *Proc. Combust. Inst.* **2000**, *28* (2), 1749−1756.

(2) Shet, H.; Parmar, U.; Bhilare, S.; Kapdi, A. R. A Comprehensive Review of Caged Phosphines: Synthesis, Catalytic Applications, and Future Perspectives. *Org. Chem. Front.* **2021**, *8* (7), 1599−1656.

(3) Manghi, M. C.; Masiol, M.; Calzavara, R.; Graziano, P. L.; Peruzzi, E.; Pavoni, B. The Use of Phosphonates in Agriculture. Chemical, Biological Properties and Legislative Issues. *Chemosphere* **2021**, *283*, 131187.

(4) Gholivand, K.; Barzegari, A.; Ghorbani-Anarkooli, M.; Malekshah, R. E.; Pourbeiranvand, S. S. Characterization, Anticancer Potential and Mechanisms of Cytotoxic Activity of Phosphoramide

Derivatives; Experimental and Theoretical Study. *Inorg. Chem. Commun.* **2025**, *174*, 113917.
(5) Gad, S. C. Phosphate Ester Flame Retardants. In *Encyclopedia of Toxicology*; Elsevier, 2014; pp. 909−912. DOI: .
(6) Li, Z. D.; Zhang, Y. C.; Xiang, H. F.; Ma, X. H.; Yuan, Q. F.; Wang, Q. S.; Chen, C. H. Trimethyl Phosphite as an Electrolyte Additive for High-Voltage Lithium-Ion Batteries Using Lithium-Rich Layered Oxide Cathode. *J. Power Sources* **2013**, *240*, 471−475.
(7) Merrow, C. N.; Nogar, N. S. Facile Infrared Laser-Induced Decomposition of Triethyl Phosphite. *Chem. Phys. Lett.* **1981**, *79* (1), 69−74.
(8) Bruce, F. N. O.; Li, Y. Probing the Thermochemistry Properties and Rate Kinetics of Trimethyl Phosphate (TMP): An H-Atom Abstraction (HAA) Reactions Perspective. *ACS Omega* **2023**, *8* (49), 47134−47145.
(9) Badhuk, P.; Ravikrishna, R. V. Development of a Skeletal Kinetic Mechanism for TMP-Based Flame Inhibition. *Combust. Theory Model.* **2022**, *26* (5), 968−987.
(10) Werner, J. H.; Cool, T. A. Kinetic Model for the Decomposition of DMMP in a Hydrogen/Oxygen Flame. *Combust. Flame* **1999**, *117* (1), 78−98.
(11) Sikes, T.; Mathieu, O.; Kulatilaka, W. D.; Mannan, M. S.; Petersen, E. L. Laminar Flame Speeds of DEMP, DMMP, and TEP Added to H2- and CH4-Air Mixtures. *Proc. Combust. Inst.* **2019**, *37* (3), 3775−3781.
(12) Neupane, S.; Barnes, F.; Barak, S.; Ninnemann, E.; Loparo, Z.; Masunov, A. E.; Vasu, S. S. Shock Tube/Laser Absorption and Kinetic Modeling Study of Triethyl Phosphate Combustion. *J. Phys. Chem. A* **2018**, *122* (15), 3829−3836.
(13) Dai, Y.; Panahi, A. Thermal Runaway Process in Lithium-Ion Batteries: A Review. *Energy* **2025**, *6*, 100186.
(14) Fu, Y.; Jiang, X.; Shi, C.; Chen, L.; Yang, Z.; Wang, M.; Hong, B.; Zhong, F.; Lai, Y. The Role of Flame-Retardant Electrolytes in Lithium-Ion Batteries: Custom Design for Improved Battery-Level Safety. *Chin. Chem. Lett.* **2025**, 110972.
(15) Zheng, D.; Peng, H.-S.; Guo, Q.-H. A Comprehensive Investigation on Both the Combustion Characteristic and Electrochemical Performance of Lithium Battery with Flame Retardant Tris (2-Chloropropyl) Phosphate. *Appl. Therm. Eng.* **2024**, *245*, 122808.
(16) Dong, Y.; Zhang, N.; Li, C.; Zhang, Y.; Jia, M.; Wang, Y.; Zhao, Y.; Jiao, L.; Cheng, F.; Xu, J. Fire-Retardant Phosphate-Based Electrolytes for High-Performance Lithium Metal Batteries. *ACS Appl. Energy Mater.* **2019**, *2* (4), 2708−2716.
(17) Li, Y.; Zhou, C.-W.; Somers, K. P.; Zhang, K.; Curran, H. J. The Oxidation of 2-Butene: A High Pressure Ignition Delay, Kinetic Modeling Study and Reactivity Comparison with Isobutene and 1-Butene. *Proc. Combust. Inst.* **2017**, *36* (1), 403−411.
(18) Glaude, P. A.; Melius, C.; Pitz, W. J.; Westbrook, C. K. Detailed Chemical Kinetic Reaction Mechanisms for Incineration of Organophosphorus and Fluoroorganophosphorus Compounds. *Proc. Combust. Inst.* **2002**, *29* (2), 2469−2476.
(19) Zhao, Y.; Truhlar, D. G. The M06 Suite of Density Functionals for Main Group Thermochemistry, Thermochemical Kinetics, Noncovalent Interactions, Excited States, and Transition Elements: Two New Functionals and Systematic Testing of Four M06-Class Functionals and 12 Other Functionals. *Theor. Chem. Acc.* **2008**, *120* (1), 215−241.
(20) Rong, C.; Zhao, D.; He, X.; Liu, S. Development and Applications of the Density-Based Theory of Chemical Reactivity. *J. Phys. Chem. Lett.* **2022**, *13* (48), 11191−11200.
(21) Montgomery, J. A.; Frisch, M. J.; Ochterski, J. W.; Petersson, G. A. A Complete Basis Set Model Chemistry. VI. Use of Density Functional Geometries and Frequencies. *J. Chem. Phys.* **1999**, *110* (6), 2822−2827.
(22) Hratchian, H. P.; Schlegel, H. B. Using Hessian Updating To Increase the Efficiency of a Hessian Based Predictor-Corrector Reaction Path Following Method. *J. Chem. Theory Comput.* **2005**, *1* (1), 61−69.
(23) Frisch, M. J.; Trucks, G. W.; Schlegel, H. B.; Scuseria, G. E.; Robb, M. A.; Cheeseman, J. R., et al. *Gaussian 16, Rev. C.01*; Gaussian, Inc.: Wallingford, CT, 2016.
(24) Cioslowski, J.; Grzebielucha, E. Zero-Point Vibrational Energies of Spherical Coulomb Crystals. *J. Chem. Phys.* **2009**, *130* (9), 094902.
(25) Lee, T. J.; Taylor, P. R. *A Diagnostic for Determining the Quality of Single-Reference Electron Correlation Methods*; NASA, 1989. https://ntrs.nasa.gov/citations/19900002238, (accessed 2025−06−05).
(26) Simmie, J. M.; Somers, K. P. Benchmarking Compound Methods (CBS-QB3, CBS-APNO, G3, G4, W1BD) against the Active Thermochemical Tables: A Litmus Test for Cost-Effective Molecular Formation Enthalpies. *J. Phys. Chem. A* **2015**, *119* (28), 7235−7246.
(27) Curtiss, L. A.; Redfern, P. C.; Raghavachari, K. Assessment of Gaussian-3 and Density-Functional Theories on the G3/05 Test Set of Experimental Energies. *J. Chem. Phys.* **2005**, *123* (12), 124107.
(28) Curtiss, L. A.; Raghavachari, K.; Redfern, P. C.; Rassolov, V.; Pople, J. A. Gaussian-3 (G3) Theory for Molecules Containing First and Second-Row Atoms. *J. Chem. Phys.* **1998**, *109* (18), 7764−7776.
(29) Curtiss, L. A.; Raghavachari, K.; Redfern, P. C.; Pople, J. A. Assessment of Gaussian-2 and Density Functional Theories for the Computation of Enthalpies of Formation. *J. Chem. Phys.* **1997**, *106* (3), 1063−1079.
(30) Namazian, M.; Coote, M. L. G3 Calculations of the Proton Affinity and Ionization Energy of Dimethyl Methylphosphonate. *J. Chem. Thermodyn.* **2008**, *40* (7), 1116−1119.
(31) Jalbout, A. F. The CH2OH+→CHO++H2 Decomposition Mechanism: A G3, G3B3, CBS-Q, CBS-QB3 versus Pure DFT Comparison: Interesting Variations. *J. Mol. Struct. THEOCHEM* **2002**, *594* (3), 129−133.
(32) Bai, X.; Li, Y.; Liu, S.; He, R.; Liang, J.; Yin, G.; Zheng, S.; Qian, Y.; Wang, X. Probing the Combustion Kinetics of Dimethylformamide: A Theoretical Study of H-Atom Abstraction Reactions. *Fuel* **2023**, *353*, 129164.
(33) Georgievskii, Y.; Miller, J. A.; Burke, M. P.; Klippenstein, S. J. Reformulation and Solution of the Master Equation for Multiple-Well Chemical Reactions. *J. Phys. Chem. A* **2013**, *117* (46), 12146−12154.
(34) Mai, T. V.-T.; Bui, T. Q.; Nhung, N. T. A.; Quy, P. T.; Shrestha, K. P.; Mauss, F.; Giri, B. R.; Huynh, L. K. An Ab Initio RRKM-Based Master Equation Study for Kinetics of OH-Initiated Oxidation of 2-Methyltetrahydrofuran and Its Implications in Kinetic Modeling. *Energies* **2023**, *16* (9), 3730.
(35) John, P. S.; Guan, Y.; Kim, Y.; Kim, S.; Paton, R. BDE-Db: A Collection of 290,664 Homolytic Bond Dissociation Enthalpies for Small Organic Molecules. *Figshare*, **2019**, .
(36) *Group Additivity Based Estimates*; 2025, Https://Webbook.Nist.Gov/Chemistry/Grp-Add/.
(37) Neale, E.; Williams, L. T. D.; Moores, V. T. 84. The Thermochemistry of Organic Phosphorus Compounds. Part II. Ester and Anilide Formation from Halides, and Combustion of the Anilides. *J. Chem. Soc.* **1956**, 422.
(38) Chernick, C. L.; Skinner, H. A.; Mortimer, C. T. Thermochemistry of Organophosphorus Compounds. Part I. Trimethyl and Triethyl Phosphites. *J. Chem. Soc.* **1955**, 3936−3938.
(39) Mortimer, C. T. The thermochemistry of organo-phosphorus compounds. *Pure Appl. Chem.* **1961**, *2* (1−2), 71−76.
(40) Ren, X.; Chen, H.; Qu, B.; Fu, X.; Liu, S.; Cao, S.; Liang, J.; Zheng, D.; Zhang, F.; Li, Y. Ab Initio Kinetics of H-Atom Abstraction from Monomethylhydrazine. *Combust. Flame* **2023**, *257*, 112998.
(41) Neupane, S.; Rahman, R. K.; Masunov, A. E.; Vasu, S. S. Theoretical Calculation of Reaction Rates and Combustion Kinetic Modeling Study of Triethyl Phosphate (TEP). *J. Phys. Chem. A* **2019**, *123* (22), 4764−4775.
(42) Dong, S.; Wagnon, S. W.; Pratali Maffei, L.; Kukkadapu, G.; Nobili, A.; Mao, Q.; Pelucchi, M.; Cai, L.; Zhang, K.; Raju, M.; Chatterjee, T.; Pitz, W. J.; Faravelli, T.; Pitsch, H.; Senecal, P. K.; Curran, H. J. A New Detailed Kinetic Model for Surrogate Fuels: C3MechV3.3. *Appl. Energy Combust. Sci.* **2022**, *9*, 100043.


https://doi.org/10.1021/acsomega.5c10154
*ACS Omega* 2026, 11, 6023−6034